Catalysis Science & Technology

ROYAL SOCIETY OF CHEMISTRY

PAPER

View Article Online
View Journal | View Issue

Cite this: *Catal. Sci. Technol.*, 2026, **16**, 2755

Design of Pt-based pseudo-binary intermetallic catalysts for dry reforming of propane using CO_2

Feilong Xing, †[a] Fang Zhang,[b] Ken-ichi Shimizu [a] and Shinya Furukawa ‡*[a]

Received 24th February 2026,
Accepted 2nd March 2026

DOI: 10.1039/d6cy00231e

rsc.li/catalysis

The utilization of CO_2 along with commercial light alkane dehydrogenation processes has attracted much attention due to the high demand for the reduction of CO_2 in the atmosphere caused by human activities and the shale gas revolution. Compared with the widely studied dry reforming of methane, converting propane to syngas using CO_2 is more beneficial in terms of easy handling, energy saving and CO_2 utilization efficiency. However, the design of an efficient and stable catalyst remains a challenge due to the difficulty of activating CO_2 and propane simultaneously. Herein, we report a multifunctional catalyst with a pseudo-binary alloy structure, Pt2CoIn3/CeO_2, which exhibits high activity for C–C bond cleavage and efficient CO_2 activation. As a result, it delivers high CO selectivity and strong coke resistance, maintaining stable performance over 100 h of reaction. Detailed X-ray analyses revealed that the intermetallic structure varies with the Co content, which in turn tunes both the C_3H_6 adsorptivity and CO_2 activation capability. By combining intermediate surface-reaction studies with density functional theory calculations, we identify the difference in the energy barriers for C_3H_6 decomposition and C_3H_6 desorption as a key descriptor governing product selectivity. These findings provide a new design concept for multimetallic catalysts that can be extended to a broad range of selective conversion reactions.

Introduction

Syngas (a mixture of H_2 and CO) production is an important industrial process for the conversion of natural gas into liquid fuels and valuable chemicals.[1] In this regard, thermochemical reforming has attracted much attention as a technology for obtaining syngas.[2–4] Conventional syngas production *via* steam reforming often yields products with $H_2:CO > 3$, which is higher than that required for further downstream processing of olefins (Fischer–Tropsch reaction) or the synthesis of oxygenated compounds. Therefore, as an alternative, the dry reforming of methane with CO_2 is highly important and thus has been extensively studied.[5–8] Recently, the dry reforming of light hydrocarbons such as ethane and propane has also received considerable attention due to the high demand for the reduction of CO_2 in the atmosphere caused by human activities and the shale gas revolution.[9–13] Compared with methane, the use of ethane and propane can consume more CO_2 stoichiometrically, thereby improving the CO_2 utilization efficiency and yielding higher H_2/CO_2 ratios,[14] which enhances their suitability for subsequent industrial applications and therefore offers great potential for reducing greenhouse gas emissions. In particular, propane is more easily activated than methane at lower reaction temperatures. Propane is generally produced by oil refinery or natural gas separation and can also be liquefied for facile storage and transportation.[13] However, due to the higher number of carbon atoms in propane than in methane, its catalytic conversion is typically prone to coking and rapid catalyst deactivation, posing challenges for the design of efficient catalysts.

There have been many previous reports on the catalytic dry reforming of propane (DRP) using precious metals such as Pt, Ru, Rh, and Re.[9,15–17] Precious metals exhibit high catalytic activity and selectivity in thermochemical reforming processes, but their high cost has limited their application in industry. Transition metal-based catalysts such as Ni are cost-effective alternatives to precious metal-based catalysts, and many researchers have studied the activity of Ni-based catalysts for dry reforming of methane reactions.[13,18–22] However, Ni-based catalysts are rapidly deactivated by sintering and coke formation,[19–25] and this is even more pronounced when Ni-based catalysts are used in DRP. Catalyst design based on multimetallic alloys is a possible

[a] *Institute for Catalysis, Hokkaido University, N21, W10, Sapporo 001-0021, Japan. E-mail: furukawa@chem.eng.osaka-u.ac.jp; Tel: +81 06 6879 7808*
[b] *Division of Applied Chemistry, Graduate School of Engineering, Osaka University, Osaka 565-0871, Japan*
† Present address: MDX Research Center for Element Strategy, Institute of Integrated Research, Institute of Science Tokyo, Yokohama 226-8503, Japan.
‡ Present address: Division of Applied Chemistry, Graduate School of Engineering, Osaka University, Osaka 565-0871, Japan.

approach to developing an efficient coke-resistant catalyst while reducing costs in large-scale processes.[26–29] Usually, it is challenging to activate both molecules simultaneously due to the different properties of propane and carbon dioxide. However, this could be overcome by combining an appropriate metal element for each molecule as a component of the alloy.[28] Recently, we reported that Pt1Co1In2/CeO_2 exhibited remarkably high catalytic activity and CO_2 utilization efficiency in the oxidative dehydrogenation of propane using CO_2 (CO_2-ODP).[27] The roles of Pt, Co, and In in the catalysis of CO_2-ODP were C_3H_8 dehydrogenation, CO_2 reduction, and enhancing C_3H_6 selectivity by the ensemble effect, respectively.

In this study, we discovered that changing the Pt : Co : In ratio in the ternary system drastically switched the product distribution from CO_2-ODP to DRP: the Co-rich PtCo2In3/CeO_2 worked as a highly efficient catalyst for DRP with high CO selectivity and long-term stability of over 100 h. By controlling the amount of Co-doping, the catalytic activity and stability of the Pt–Co–In/CeO_2 catalyst can be largely improved. The origin of the "switching catalysis" was investigated by a mechanistic study based on some characterization techniques such as X-ray powder diffraction (XRD), transmission electron microscopy (TEM), and temperature-programmed-mass spectrometry measurements (TP-MS). Here, we report not only a highly efficient catalyst for DRP with high selectivity, coke resistance, and thermal stability, but also the high tunability of catalyst design based on the multi-metallic alloys.

Results

Structure characterization of the catalysts

The Pt–Co–In/CeO_2 (Pt: 3 wt%, Pt : Co : In = 1 : 2 : 3 and 2 : 1 : 3, hereafter, PtCo2In3 and Pt2CoIn3) catalysts were prepared by a conventional impregnation method using CeO_2 as a support. The catalyst was first characterized by high-angle annular dark-field scanning transmission electron microscopy (HAADF-STEM) and energy dispersive X-ray (EDX) analyses (Fig. 1a and S1). The elemental maps of Pt, Co, and In confirmed that these three elements were highly dispersed on the support and comprised the nanoparticles with a diameter of ~5 nm. Other Co species were also present apart from those in the alloy nanoparticles. To confirm whether Co was doped into the nanoparticles, X-ray diffraction (XRD) analysis (Fig. 1b and S2a) was performed. The referenced PtIn/CeO_2 showed two intense peaks assignable to the 110 and 102 diffractions of intermetallic Pt_2In_3 ($P\bar{3}m1$, ICSD-197672) at 39.7° and 40.0°, respectively (Fig. S2a). These peaks slightly shifted to lower angles when a small amount of Co was added (39.6° and 39.9°, Fig. 1b, Pt2CoIn3/CeO_2), indicating the lattice shrinkage of Pt_2In_3 upon Co-doping and the formation of the $(Pt_{1-x}Co_x)_2In_3$ pseudo-binary alloy structure. When the Co ratio was further increased (PtCo2In3/CeO_2), diffraction peaks assignable to the $PtIn_2$-

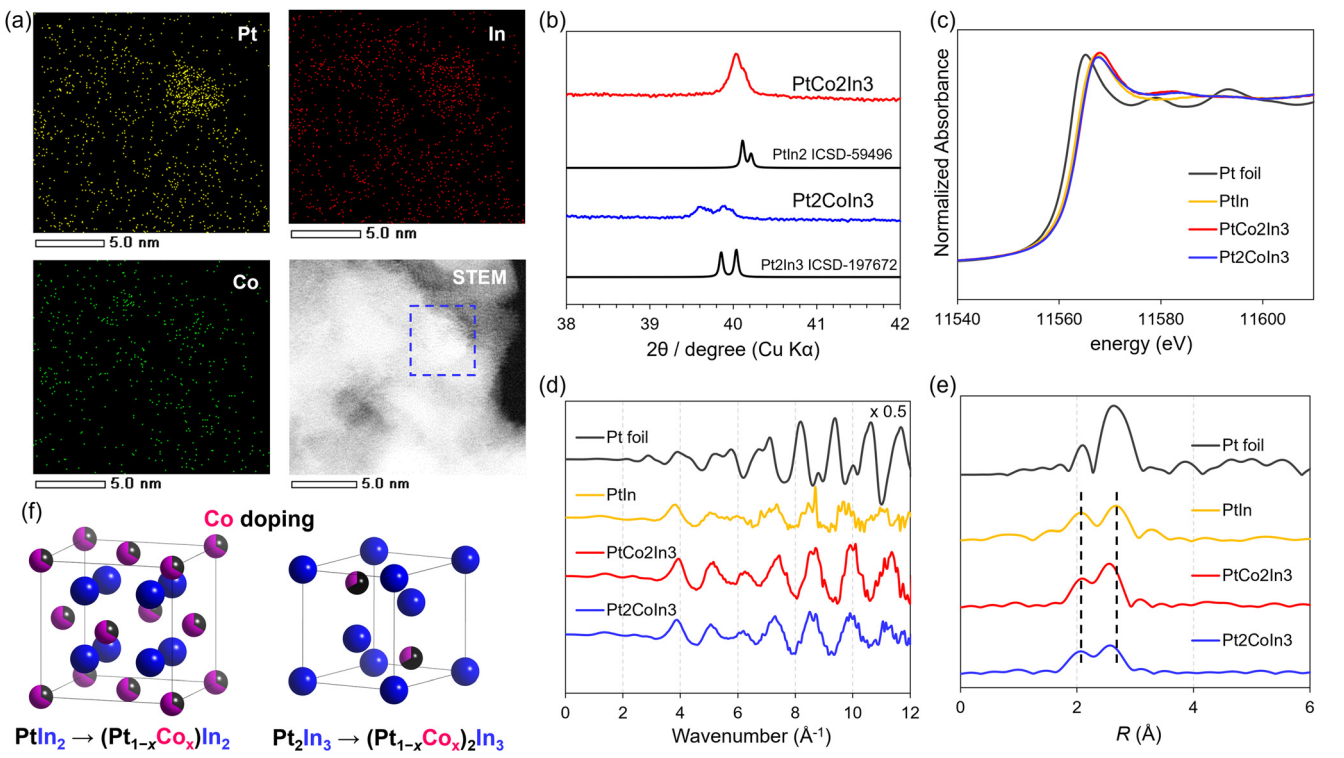

Fig. 1 Characterization of Pt–Co–In/CeO_2: (a) elemental maps of Pt, Co, In, overlap, and the HAADF-STEM image of Pt–Co–In/CeO_2 (Pt : Co : In = 1 : 2 : 3). (b) XRD patterns of PtCo2In3/CeO_2 and Pt2CoIn3/CeO_2. (c) Pt L_{III}-edge XANES, (d) EXAFS, and (e) FT-EXAFS of the Pt foil, PtIn/CeO_2, Pt2CoIn3/CeO_2, and PtCo2In3/CeO_2. (f) Single unit cells of the $(Pt_{1-x}Co_x)In_2$ and $(Pt_{1-x}Co_x)_2In_3$ pseudo-binary alloy structures.

like ($Fm\bar{3}m$, ICSD-59496) structure appeared at 40.0° and 40.1°, which were slightly lower than those of the corresponding pure $PtIn_2$ (40.1° and 40.2°, respectively). This indicates that Co had been doped into the lattice of $PtIn_2$ intermetallic structures, forming a $(Pt_{1-x}Co_x)In_2$ pseudo binary alloy phase. The crystal structure of Pt–In intermetallics changed depending on the Co content. To determine the crystallographic site of Co, X-ray absorption fine structure (XAFS) analysis was carried out. The Pt L_{III}-, Co K- and In K-edge X-ray adsorption near-edge structure (XANES) spectra of the Pt-based catalysts showed white line intensities similar to those of the reference foil (Fig. 1c), which confirmed that these metals were in the metallic states. The Pt L_{III}-edge adsorption edges shifted to high energy (Fig. S3a), which could contribute to the electron transfer by alloying with Co and In. The electronic state of surface Pt was further examined by XPS (Fig. S2b). The Pt 4f peak of monometallic Pt was located at ~71.0 eV, consistent with the reported binding energy of metallic Pt.[30–32] In contrast, the PtIn intermetallic catalysts exhibited a positive shift to higher binding energy, attributable to alloying-induced electronic modification, in agreement with the XANES results. Moreover, increasing Co-doping resulted in a further slight positive shift of the Pt 4f peaks, indicating the progressive modulation of the Pt electronic environment, which may influence reactant adsorption. A small fraction of In_2O_3 was observed in the In K-edge XANES (Fig. S3d) and extended XAFS (EXAFS) spectra (Fig. S3e; the Fourier

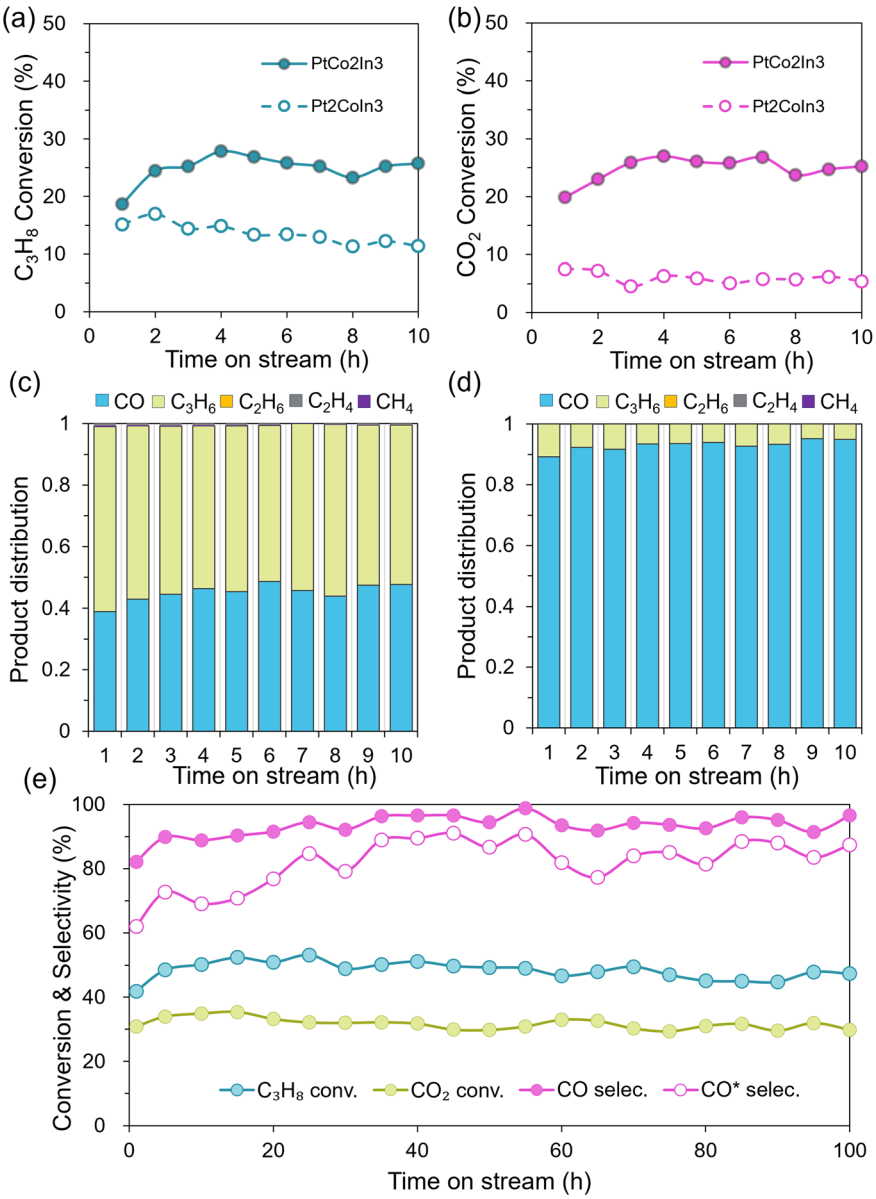

Fig. 2 Catalytic performance of Pt–Co–In/CeO_2 in DRP: time course of (a) C_3H_8 conversion and (b) CO_2 conversion. Product distribution of (c) Pt2CoIn3/CeO_2 and (d) PtCo2In3/CeO_2. (e) Long-term stability testing with the PtCo2In3/CeO_2 catalyst: time course of C_3H_8 and CO_2 conversions, CO selectivity and CO* net selectivity.

transform of the EXAFS (FT-EXAFS) is shown in Fig. S3f), probably due to the high-oxophilicity with the lattice oxygen of CeO_2. Fig. 1d shows the Pt L_{III}-edge EXAFS raw oscillation features of Pt foil and the corresponding catalysts. PtCo2In3/CeO_2 and Pt2CoIn3/CeO_2 exhibited similar features to those of PtIn/CeO_2, but were different from the reference Pt foil having an fcc structure. Similar trends were also shown in the Co K-edge and In K-edge spectra (Fig. S3b and e). These results indicate that the locations of the transition metal (Pt and Co) and the typical metal (In) atoms in the Pt–Co–In/CeO_2 catalysts were crystallographically altered, which is consistent with the XRD results (Fig. 1b). Fig. 1e shows the Pt L_{III}-edge FT-EXAFS spectra of the Pt-based catalysts. The peak position of Pt–In scattering in Pt–Co–In/CeO_2 was shorter than that in PtIn/CeO_2, suggesting that the lattice distortion resulted from Co-doping. Importantly, the EXAFS curve-fitting was successfully done, considering the Pt–In (In–Pt) and Co–In (In–Co) scatterings, whereas no reliable fitting was obtained when Pt–Co (Co–Pt) scatterings were considered (Fig. S4 and Table S1). This strongly supports the site-selective doping of Co into the Pt sites and demonstrates the formation of the pseudo-binary alloy structure on the CeO_2 support. Co–Co scattering was also observed, obtained in the Co K-edge, which may be attributed to monometallic Co species that did not participate in the alloy formation; this is consistent with the observation in the HAADF-STEM-EDX analysis.

Catalytic performance in DRP

The prepared PtCo2In3/CeO_2 and Pt2CoIn3/CeO_2 catalysts were then tested in CO_2-assisted propane conversion with a C_3H_8 : CO_2 molar ratio of 1 : 3 at 550 °C. Fig. 2a–d show the time course of C_3H_8 conversion, CO_2 conversion and the product distribution of both catalysts, respectively. The Pt2CoIn3/CeO_2 showed a C_3H_6-rich product distribution that consisted of 60% C_3H_6, 39% CO, and the other C_{1-2} products, and C_3H_6 selectivity remained at 52% after a 10 h reaction. In contrast, the PtCo2In3/CeO_2 catalyst was CO-dominant; CO selectivity was 89% at the initial stage and increased to 95% after a 10 h reaction. This suggests that PtCo2In3/CeO_2 has a higher dry reforming activity, likely due to its strong propensity for C–C bond cleavage and subsequent oxygenation, whereas Pt2CoIn3/CeO_2 preferentially produces C_3H_6 *via* C–H bond cleavage and facile desorption. Differences were also observed in the C_3H_8 conversion trend over time. Although the initial C_3H_8 conversion was similar for PtCo2In3/CeO_2 and Pt2CoIn3/CeO_2 (~16%, Fig. 2a), C_3H_8 conversion increased after 10 h of reaction and stabilized at ~26% for PtCo2In3/CeO_2, whereas it gradually decreased to ~10% for Pt2CoIn3/CeO_2. To understand the individual effect of each second metal, we also performed control experiments using the corresponding monometallic (Pt/CeO_2) and bimetallic (PtCo/CeO_2, Co-rich PtCo3/CeO_2, PtIn/CeO_2, and In-rich PtIn3/CeO_2) catalysts (Fig. S5). C_3H_8 conversion for Pt/CeO_2, PtCo/CeO_2, and PtIn/CeO_2 was 40%, 33%, and 28%, while the CO_2 conversion was 38%, 40%, and 16%, respectively. The Co-rich PtCo3/CeO_2 exhibited high initial conversions of both C_3H_8 and CO_2, likely due to the strong C–C cleavage ability of the Co-rich PtCo alloy and/or the large amount of remaining Co species. In contrast, In-rich PtIn3/CeO_2 showed low conversions of C_3H_8 and CO_2, which may be attributed to the blocking of the active sites by unalloyed In species. These results show that alloying Pt with Co or In decreases C_3H_8 conversion due to the ensemble effect, while adding a certain amount of Co increases CO_2 conversion. Furthermore, Pt2CoIn3/CeO_2 displayed a similar product distribution to that of PtIn/CeO_2, indicating that adding only a small amount of Co did not significantly affect the inherent product distribution of PtIn/CeO_2. All the catalysts except PtCo2In3/CeO_2 were rapidly deactivated, highlighting that PtCo2In3/CeO_2 not only showed superior activity in the dry reforming reaction but also had excellent stability. To identify the alloying effect of PtCo2In3/CeO_2, we further tested the control experiments (Fig. S6) using physical mixtures of the binary and monometallic catalysts (Pt/CeO_2 + Co–In/CeO_2) and tandem catalytic systems with two sequential catalyst beds (Pt/CeO_2 → glass wool → Co–In/CeO_2 and CoIn/CeO_2 → glass wool → Pt/CeO_2). The physical mixture test showed lower catalytic activity than PtCo2In3/CeO_2, while the tandem system exhibited lower stability, suggesting that the ternary alloy based on the pseudo-binary structure is essential for high catalytic performance. Then, we examined the long-term stability of PtCo2In3/CeO_2, which showed a remarkably high stability: the conversion of C_3H_8 and CO_2 did not decrease, even at 100 h, while maintaining ~95% CO selectivity and ~87% net CO selectivity. In contrast to conventional systems that require high temperatures or high CO_2/propane ratios for considerable conversion (Table S2), the developed catalyst achieved a high propane consumption rate under mild, energy-efficient conditions. It maintained a high reaction rate while exhibiting excellent durability and coke resistance, addressing the challenges of low-temperature dry reforming. To verify the reason for the long-term stability, temperature-programmed oxidation (TPO, Fig. S7) and XRD analyses (Fig. S8) of the spent catalysts after 50 h catalytic run were conducted. As verified by O_2-TPO of the fresh monometallic Pt, bimetallic PtIn, and $PtCo_2In_3$ catalysts (Fig. S7c), the O_2 consumption of the fresh samples was below the detection limit, indicating that the O_2 uptake and the corresponding CO_2 evolution observed for the spent catalysts mainly reflect the combustion of deposited coke and are not dominated by the oxidation of intrinsic defects from the supports. The amount of coke shown in Fig. 3a was quantified by integrating the CO_2 signal (Fig. S7b) throughout the entire TPO run. For clear comparison, the catalyst exhibiting the largest integrated TPO peak area (PtIn/CeO_2) was defined as 100, and the integrated areas of the other catalysts were normalized to this value. The relative coke amount on PtCo2In3/CeO_2 was much lower than that on Pt/CeO_2, PtCo/CeO_2, and PtIn/CeO_2, even after 50 h reaction (Fig. 3a). On the other hand, the physical mixture of the binary and

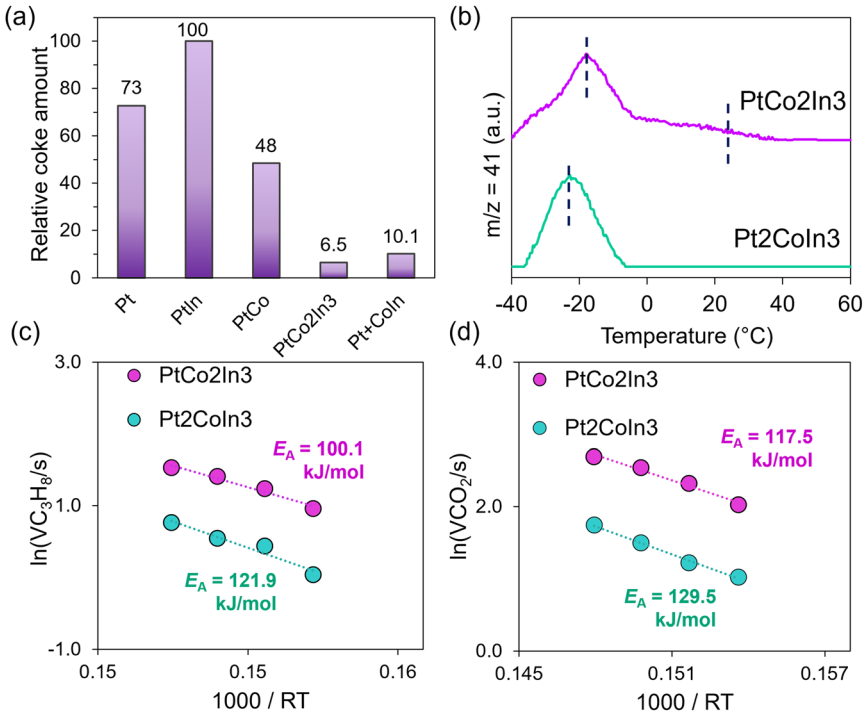

Fig. 3 (a) Relative coke amounts accumulated on the catalysts, estimated from O_2-TPO profiles of the spent catalysts after 50 h of DRP at 550 °C. (b) C_3H_6-TPD for PtCo2In3/CeO_2 and Pt2CoIn3/CeO_2. Catalysts (adsorption temperature: −35 °C). Arrhenius-type plots for (c) C_3H_8 and (d) CO_2 conversion rates obtained in DRP on PtCo2In3/CeO_2 and Pt2CoIn3/CeO_2 catalysts. The catalyst amount was set to 20 mg to ensure that the conversion was below 15%.

monometallic catalysts (Pt/CeO_2 + Co–In/CeO_2) also exhibited a quite low coke amount, which was only slightly higher than that of PtCo2In3/CeO_2. On combining these results, we conclude that the close contact of Pt, Co, and In at an atomic level is necessary to minimize coke accumulation. A possible explanation is that the proximity of the three metal elements Pt–Co–In allows facile coupling of C and O atoms generated by C–C scission on the Pt–Co sites[33] and by CO_2 activation on the Co–In sites,[27] respectively, at their interface.

Mechanistic study

Next, a mechanistic study was conducted to elucidate the origin of the difference in selectivity and stability between PtCo2In3/CeO_2 and Pt2CoIn3/CeO_2 catalysts. The apparent activation energy (Fig. 3c and d) was evaluated using Arrhenius-type plots. Compared with the Pt2CoIn3/CeO_2, the activation energies of PtCo2In3/CeO_2 for C_3H_8 and CO_2 decreased from 121.9 to 100.1 kJ mol^{-1} and 129.5 to 117.5 kJ mol^{-1}, respectively. This suggests that adjusting the amount of Co in the PtIn crystal structure could reduce the activation barrier, which is consistent with the activity trend in the DRP reaction. Then, we performed a kinetic study on the CO_2-DRP reaction over PtCo2In3/CeO_2 at 550 °C within the Arrhenius temperature window. The reaction order of $P_{C_3H_8}$ is positive for both $r_{C_3H_8}$ and r_{CO_2} (0.69 and 1.31; Fig. S9c and d), whereas that of P_{CO_2} is negative for r_{CO_2} (−0.47; Fig. S9a) and near-zero for $r_{C_3H_8}$ (−0.02; Fig. S9b). This near-zero to negative dependence suggests that increasing P_{CO_2} does not accelerate the rate in the investigated range and can even suppress CO_2 consumption, which is consistent with competitive adsorption by CO_2-derived surface species. This behavior suggests that the overall rate is primarily governed by steps associated with propane activation/dehydrogenation, whereas the influence of CO_2 partial pressure on propane consumption rate is negligible under these conditions. To further determine the reason for the different selectivities of these two catalysts, temperature-programmed surface reactions (TPSRs) were conducted under various conditions, such as C_3H_6 desorption (C_3H_6-TPD), propylene oxidation by CO_2 (C_3H_6 + CO_2), and reverse water-gas shift reaction (RWGS, H_2 + CO_2). From the C_3H_6-TPD results (Fig. 3b), PtCo2In3 exhibited a broad desorption feature between −40 and 40 °C, whereas Pt2CoIn3 showed a single sharp peak at around −30 °C and almost complete desorption by this temperature. The broader and slightly higher-temperature desorption on PtCo2In3 suggests the stronger and more heterogeneous adsorption of C_3H_6, while Pt2CoIn3 binds C_3H_6 more weakly and thus favors the facile desorption of propylene once it is formed from propane dehydrogenation. TPD reflects adsorption stability under inert conditions; stronger C_3H_6 adsorption on PtCo2In3 therefore implies longer surface residence and a higher probability for subsequent surface reactions, whereas rapid desorption on P2tCoIn3 limits further transformation. To further elucidate the effect of Co content on the subsequent transformation of

reaction intermediates, C_3H_6 + CO_2 TPSR experiments were performed. C_3H_6 starts to be consumed at around 350 °C over PtCo2In3, whereas a higher temperature is required over Pt2CoIn3. This indicates that the strongly adsorbed C_3H_6 species on PtCo2In3 are more readily activated toward subsequent oxidation/reforming, leading to the higher formation of CO, H_2O, and H_2, which aligns well with the C_3H_6 selectivity trend. Moreover, the easier transformation of C_3H_6 over PtCo2In3 is accompanied by enhanced CO_2 activation, as evidenced by the larger decrease in the m/z = 44 signal. Confirmed by the following H_2 + CO_2 TPSR experiments, PtCo2In3 shows slightly higher consumption of H_2 and CO_2 and higher production of CO and H_2O than Pt2CoIn3 (Fig. 4b), pointing to a more efficient RWGS pathway. Overall, PtCo2In3 exhibits higher activity and selectivity for dry reforming than Pt2CoIn3, which can be attributed to the kinetically more favorable activation/dehydrogenation of C_3H_6 due to the stronger C_3H_6 adsorption capability, and the more efficient RWGS reaction by verifying the Co-content.

Density functional theory (DFT) calculations were conducted to obtain atomic-scale insight into the selectivity switching trend between Pt2CoIn3 and PtCo2In3 catalysts depending on their specific surface structure. The Pt_2In_3(012) and $PtIn_2$(111) planes were selected as the models of Pt2CoIn3 and PtCo2In3, respectively, because they are the most stable surfaces having high surface atomic densities, hence the strong diffraction as shown in Fig. 1b. The reaction environments of the Co-doped pseudo-binary alloy catalysts (Pt2CoIn3 and PtCo2In3) were modeled as Pt_2In_3(012)–Co and $PtIn_2$(111)–Co, respectively, by replacing surface Pt atoms of the Pt_2In_3 (012) and $PtIn_2$(111) slab models with Co atoms. Fig. 5a shows the transition state (TS) of the C_3H_6 decomposition to C_3H_5 + H on Pt_2In_3(012)–Co (left) and on $PtIn_2$(111)–Co (right) surfaces. The difference in the energy barriers (ΔE = E_a − E_d) of C_3H_6 decomposition (E_a) and desorption (E_d) was used as a scale for evaluating the selectivity trend (Fig. 5b). Pt_2In_3(012)–Co exhibited high E_a and low E_d, thus providing large ΔE and favoring the dehydrogenation step. In contrast, $PtIn_2$(111)–Co showed very low ΔE due to moderate E_a and high E_d, which easily induced the decomposition process leading to dry reforming. This trend agrees well with the experimental selectivity trend. The change in the surface structure originating from the bulk crystal structures plays a crucial role in determining the fate of C_3H_6—whether it desorbs to dehydrogenation or decomposes to reforming. The stronger adsorption capability of the PtCo2In3 surface suggests that dry reforming primarily

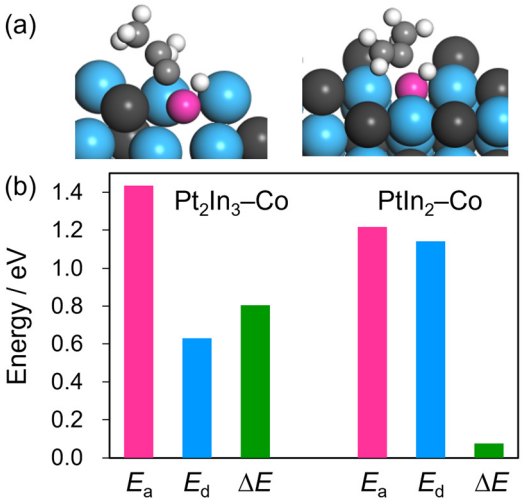

Fig. 5 (a) TS of the C_3H_6 decomposition to C_3H_5 + H on the Pt_2In_3(012)–Co (left) and $PtIn_2$(111)–Co (right) surfaces. (b) Energy barriers of the C_3H_6 decomposition (E_a), C_3H_6 desorption (E_d), and the difference between E_a and E_d (ΔE).

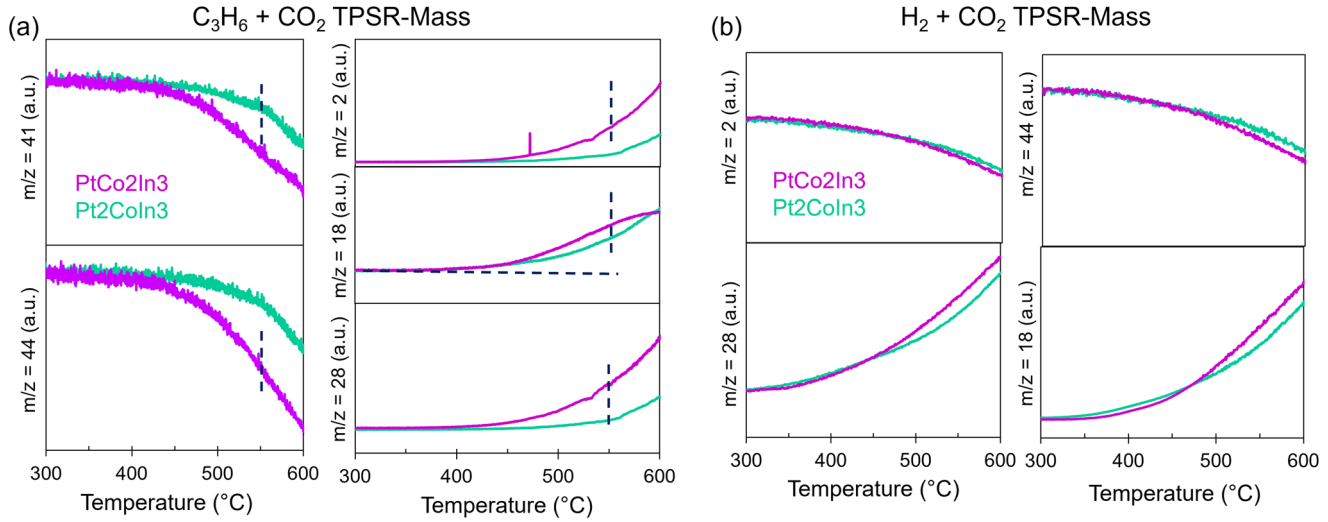

Fig. 4 Temperature-programmed surface reactions (TPSRs) on the PtCo2In3/CeO_2 and Pt2CoIn3/CeO_2 catalysts. (a) C_3H_6 + CO_2 TPSR-mass experiments (b) and H_2 + CO_2 TPSR-mass experiments. The reactants and products were collected with the mass intensity of m/z = 2(H_2), m/z = 18(H_2O), m/z = 28(CO), m/z = 41(C_3H_5), and m/z = 44(CO_2).

occurs *via* C_3H_6 without changing the main reaction mechanism, while just altering the product distribution.

Conclusion

Overall, we have designed a highly efficient ternary PtCo2In3/CeO_2 catalyst for the DRP reaction with high selectivity and stability, even for a 100 h reaction. The results showed that the catalytic behavior of PtCo2In3/CeO_2 and Pt2CoIn3/CeO_2 catalysts is highly sensitive to the doping amount of Co. Comprehensive structural characterization (X-ray techniques and TEM) showed that increasing the Co content drives an intermetallic phase evolution from Pt_2In_3 ($P\bar{3}m1$) to PtIn2 ($Fm\bar{3}m$). By controlling the amount of Co-doping, the catalytic properties of Pt–Co–In/CeO_2 can be drastically switched from "CO_2-ODP-dominant" to "DRP-specific". TPSR experiments and DFT calculations further revealed that, compared with Pt2CoIn3/CeO_2, PtCo2In3/CeO_2 exhibits stronger adsorptivity of C_3H_6 and lower activation energy of CO_2, thus facilitating the subsequent decomposition of propylene into CO. Herein, we report an excellent catalyst for DRP that opens up a new avenue for catalyst design concepts based on multi-metallic catalysts. The obtained insights and technology will contribute to the carbon-neutralization of industrial processes for light alkane conversion.

Experiments

Catalyst preparation

Pt/CeO_2, Pt–Co/CeO_2, Pt–In/CeO_2, and Pt–Co–In/CeO_2 (Pt: 3 wt%) were prepared by a conventional impregnation method using H_2PtCl_6 (aqueous solution, Kojima Chemicals, Pt 8.77 wt%), $In(NO_3)_3{\cdot}3H_2O$, and $Co(NO_3)_2{\cdot}6H_2O$, as metal precursors. The CeO_2 support (JRC-CEO-2, S_{BET} = 123.1 m^2g^{-1}) was added to a vigorously stirred aqueous solution (50 mL H_2O per gram of CeO_2) containing Pt and the corresponding second and/or third metal precursor(s) (Pt : Co = 1 : 1, Pt : In = 1 : 1, and Pt : Co : In = 1 : 2 : 3 or 2 : 1 : 3), followed by stirring for 3 h at room temperature. The mixture was dried under reduced pressure at 50 °C using a rotary evaporator, followed by calcination under flowing air at 500 °C for 1 h and reduction under flowing H_2 (50 mL min^{-1}) at 600 °C for 1 h. Co/CeO_2, CoIn/CeO_2, and In/CeO_2 were prepared by a similar method, where the amounts of Co and In were adjusted to be equal to those included in Pt–Co–In/CeO_2.

Catalytic test

DRP was performed in a quartz fixed-bed reactor with an internal diameter of 6 mm under atmospheric pressure. The catalysts (0.10 g) were diluted with sea sand (0.90 g, Miyazaki Chemical, 99.9%) and treated under flowing hydrogen (10 mL min^{-1}) at 550 °C for 0.5 h prior to the catalytic reactions. The catalysts were then evaluated by feeding the reactant gas mixture ($C_3H_8 : CO_2 : He$ = 1 : 3 : 2) with a total flow rate of 30 mL min^{-1}. The 100 h long-time stability reaction was test by feeding reactant gas mixture ($C_3H_8 : CO_2 : He$ = 1 : 3 : 26) at the same total flow rate. The gas phase was analyzed and quantified using an online thermal conductivity detection gas chromatograph (Shimadzu GC-8A, column: Gaskuropack 54) equipped downstream. For all the catalysts, C_3H_6, C_2H_4, C_2H_6, CH_4, CO, CO_2, H_2O, and H_2 were detected as reaction products in outlet gas.

$$C_3H_8 \text{ conversion: } X_{C_3H_8}(\%) = \frac{F^{in}_{C_3H_8} - F^{out}_{C_3H_8}}{F^{in}_{C_3H_8}} \times 100 \quad (1)$$

$$CO_2 \text{ conversion: } X_{CO_2}(\%) = \frac{F^{in}_{CO_2} - F^{out}_{CO_2}}{F^{in}_{CO_2}} \times 100 \quad (2)$$

F^{in}_x and F^{out}_x indicate the inlet and outlet flow rates of x (mL min^{-1}), respectively.

In this reaction, CO can be generated from C_xH_y species *via* dry reforming as well as from the oxidative dehydrogenation of propane. To distinguish between these pathways, we have defined two separate expressions for CO selectivity.

Product selectivity, including CO selectivity, is defined on a carbon number basis with respect to product-derived carbon:

$$C_xH_y{:}S^{out}_{C_xH_y}(\%) = \frac{xF^{out}_{C_xH_y}}{F^{out}_{C_3H_6} + \frac{2}{3}F^{out}_{C_2H_6} + \frac{2}{3}F^{out}_{C_2H_4} + \frac{1}{3}F^{out}_{CH_4} + \frac{1}{3}F^{out}_{CO}} \times 100 \quad (3)$$

$$CO{:}S^{out}_{CO}(\%) = \frac{\frac{1}{3}F^{out}_{CO}}{F^{out}_{C_3H_6} + \frac{2}{3}F^{out}_{C_2H_6} + \frac{2}{3}F^{out}_{C_2H_4} + \frac{1}{3}F^{out}_{CH_4} + \frac{1}{3}F^{out}_{CO}} \times 100 \quad (4)$$

Net CO selectivity (CO* selec.): CO selectivity generated from propane *via* the dry reforming of propane can be defined as the ratio of the carbon atoms, like this: $\left[F^{C_xH_y}_{CO} = \frac{\frac{1}{3}F^{out}_{CO} - F^{out}_{C_3H_6}}{2}\right]$.

$$C_3H_6 \text{ sel. in } C_xH_y{:}S^{C_xH_y}_{C_3H_6}(\%) = \frac{F^{out}_{C_3H_6}}{F^{out}_{C_3H_6} + \frac{2}{3}F^{out}_{C_2H_6} + \frac{2}{3}F^{out}_{C_2H_4} + \frac{1}{3}F^{out}_{CH_4} + F^{C_xH_y}_{CO}} \times 100 \quad (5)$$

$$CO^*{:}S^{C_xH_y}_{CO_{net}}(\%) = \frac{F^{C_xH_y}_{CO}}{F^{out}_{C_3H_6} + \frac{2}{3}F^{out}_{C_2H_6} + \frac{2}{3}F^{out}_{C_2H_4} + \frac{1}{3}F^{out}_{CH_4} + F^{C_xH_y}_{CO}} \times 100 \quad (6)$$

The carbon balance (including unreacted C_3H_8 and CO_2 and all GC-detectable carbon-containing products) closed within 95–105%. Total carbon balance (CB) was defined as follows:

$$CB = \frac{F^{out}_{C_3H_8} + F^{out}_{C_3H_6} + \frac{2}{3}F^{out}_{C_2H_6} + \frac{2}{3}F^{out}_{C_2H_4} + \frac{1}{3}F^{out}_{CH_4} + \frac{1}{3}F^{out}_{CO_2} + \frac{1}{3}F^{C_xH_y}_{CO} + \frac{1}{3}F^{CO_2}_{CO}}{F^{in}_{C_3H_8} + \frac{1}{3}F^{in}_{CO_2}} \times 100 \quad (7)$$

Characterization

The crystal structure of the prepared catalyst was examined *via* powder X-ray diffraction (XRD) using a Rigaku MiniFlex II/AP diffractometer with Cu Kα radiation. High-angle annular dark field scanning transmission electron microscopy (HAADF-STEM) was carried out using a JEOL JEM-ARM200 M microscope equipped with an energy dispersive X-ray (EDX) analyzer (EX24221M1G5T). STEM analysis was performed at an accelerating voltage of 200 kV. To prepare the TEM specimen, all samples were sonicated in ethanol and then dispersed on a Mo grid supported by an ultrathin carbon film.

The TPO experiment was conducted using BELCAT II (MicrotracBEL) to quantify the amount of coke deposited on the spent catalysts after 50 h of DRP at 550 °C (0.1 g of the catalyst with 0.9 g quartz sand). The spent catalyst was placed in a quartz tube reactor and treated under flowing He (30 mL min^{-1}) at 150 °C for 30 min, followed by cooling to room temperature. The catalyst bed temperature was then increased (40–900 °C, ramping rate: 5 °C min^{-1}) under flowing O_2/He (2%, 50 mL min^{-1}). The amount of CO_2 in the outlet gas was quantified using an online mass spectrometer. C_3H_6 and CO_2 temperature-programmed desorption were performed. Prior to the C_3H_6-TPD, the as-reduced catalyst (100 mg) was heated to 600 °C under a 5%H_2/Ar gas mixture (20 mL min^{-1}) with a ramping rate of 20 °C min^{-1}, then kept at the same temperature for 0.5 h. After the reduction, the catalyst was cooled to −35 °C using CATCryo-II under a He flow (20 mL min^{-1}), kept at −35 °C for 0.5 h, and subsequently exposed to 5% C_3H_6/He gas mixture (20 mL min^{-1}) at the same temperature for 5 min. The catalyst was then purged under He (50 mL min^{-1}) at −35 °C for 1.5 h, and subsequently heated from −35 °C to 300 °C with a ramping rate of 2 °C min^{-1}. The outlet gas (C_3H_6; m/z = 41) was analyzed online using a quadrupole mass spectrometer (BELMASS). For C_3H_6 + CO_2-TPSR, the catalyst was pre-treated under a 5%H_2/Ar gas mixture (20 mL min^{-1}) at 600 °C, purged under He (50 mL min^{-1}) at 50 °C for 0.5 h, and subsequently heated from 50 °C to 600 °C at a ramping rate of 5 °C min^{-1} with C_3H_6 + CO_2 gases (5 + 15 mL min^{-1}) flowing downstream of the catalyst bed. The outlet gas (CO_2; m/z = 44, C_3H_6; m/z = 41, CO; m/z = 28, H_2O; m/z = 18, and H_2; m/z = 2) was analyzed online by a quadrupole mass spectrometer (MicrotracBEL, BELMASS).

XPS (Kratos-ULTRA2, Shimadzu) analysis was conducted using an air-isolated sample vessel and an apparatus equipped with a charge neutralization system. The binding energy was corrected against the signal of the C 1s orbital (C 1s = 284.6 eV). Before the measurement, the catalyst was pretreated with H_2 (30 mL min^{-1}) at 550 °C for 2 h in a quartz tube, followed by cooling to room temperature, purging with Ar (10 mL min^{-1}) and storing in the glovebox. X-ray absorption fine structure (XAFS) spectra of the prepared catalysts were obtained at the BL01B14 beamline of SPring-8, Japan Synchrotron Radiation Research Institute (JASRI), using Si(111) (for Co K- and Pt L_{III}-edges) and Si(311) (for In K-edge) double-crystals as monochromators. Prior to the measurement, the catalyst was pelletized (*ca.* 150 mg with a diameter of 10 mm) and pretreated with H_2/N_2 (20%, 40 mL min^{-1}) at 550 °C for 0.5 h in an *in situ* quartz cell, followed by cooling to room temperature with N_2 purge (50 mL min^{-1}). The XAFS spectra were recorded in transmission (In K-edge) and fluorescence (Pt L_{III}-, and Co K-edge: using a 19-element Ge solid-state detector) modes at room temperature. Athena and Artemis software ver. 0.9.25, implemented in the Demeter package, were used for the analysis of the obtained XAFS spectra. FEFF8 was used for the calculation of the back-scattering amplitude and phase shift functions.[34] We defined the *R*-factor (R^2) for curve-fitting as follows: $R^2 = \sum_i \{k^3\chi_i^{exp}(k) - k^3\chi_i^{fit}(k)\}^2 / \sum_i \{k^3\chi_i^{exp}(k)\}^2$.

Computational details

Periodic DFT calculations were performed using the CASTEP code[35] with Vanderbilt-type ultrasoft pseudopotentials, as well as the revised version of the Perdew–Burke–Ernzerhof exchange–correlation functional based on the generalized gradient approximation.[36] At a kinetic energy of 360 eV, the plane-wave basis set was truncated. A 0.1 eV Fermi smearing was utilized. The Tkatchenko–Scheffler method was used to analyze dispersion correlations with a scaling coefficient of s_R = 0.94 and a damping parameter of d = 20.[37] The reciprocal space was sampled using a *k*-point mesh with a spacing of typically 0.04 $Å^{-1}$, as generated by the Monkhorst–Pack scheme.[38] Geometry optimizations and transition state (TS) searches were performed on supercell structures using periodic boundary conditions. The surfaces were modeled using metallic slabs with a thickness of four atomic layers with 13 Å of vacuum spacing. Geometry optimizations were performed using the two-point steepest descent (TPSD) algorithm.[39] We chose Pt_2In_3(012) and $PtIn_2$(111) as the most stable surfaces (Pt2CoIn3 and PtCo2In3, respectively), which have high surface atom density and diffraction intensity.[40,41] Pt_2In_3(012)–Co and $PtIn_2$(111)–Co were constructed as models of the surface pseudo binary alloy by replacing one of the surface Pt atoms of Pt_2In_3(012) and $PtIn_2$(111)–Co. The unit cell sizes of the bulk materials (Pt_2In_3(012)–Co and $PtIn_2$(111)–Co) were first optimized, followed by modeling the slab structure and surface relaxation with the size of the supercell fixed. The convergence criteria for structure optimization and energy calculation were set to (a) an SCF tolerance of 1.0×10^{-6} eV

per atom, (b) an energy tolerance of 1.0×10^{-5} eV per atom, (c) a maximum force tolerance of 0.05 eV Å^{-1}, and (d) a maximum displacement tolerance of 1.0×10^{-3} Å.

The adsorption energy was defined as follows: $E_{ad} = E_{A\text{-}S} - (E_S + E_A)$, where $E_{A\text{-}S}$ is the energy of the slab together with the adsorbate, E_A is the total energy of the free adsorbate, and E_S is the total energy of the bare slab. The adsorption energy for an oxygen-preadsorbed slab was calculated using E_{SH}, which is the total energy of the oxygen-adsorbed slab, instead of using E_S.

The transition state (TS) search was performed using the complete linear synchronous transit/quadratic synchronous transit (LST/QST) method.[42,43] Linear synchronous transit maximization was performed, followed by energy minimization in the directions conjugate to the reaction pathway. The approximated TS was used to perform QST maximization with conjugate gradient minimization refinements. This cycle was repeated until a stationary point was found. Convergence criteria for the TS calculations were set to root-mean-square forces on an atom tolerance of 0.05 eV Å^{-1}.

Conflicts of interest

The authors declare no competing interests.

Data availability

All data supporting the findings of this study are available within the article and its supplementary information (SI).

Supplementary information is available. See DOI: https://doi.org/10.1039/d6cy00231e

Acknowledgements

This work was supported by JSPS KAKENHI (Grant Numbers 22KJ0077, 22J11748, 17H01341, 17H04965, 25K23522, and 20H02517) and JST PRESTO (JPMJPR19T7). The XAFS analysis was performed with the approval of JASRI (No. 2021B1962 and 2022A0302). We appreciate the technical staffs of the Faculty of Engineering, Hokkaido University, and of the Research Institute for Electronic Science, Hokkaido University, for their assistance with HAADF-STEM observation.

References

1 D. Pakhare and J. Spivey, A Review of Dry (CO_2) Reforming of Methane over Noble Metal Catalysts, *Chem. Soc. Rev.*, 2014, **43**(22), 7813–7837.
2 L. Zhong, F. Yu, Y. An, Y. Zhao, Y. Sun, Z. Li, T. Lin, Y. Lin, X. Qi, Y. Dai, L. Gu, J. Hu, S. Jin, Q. Shen and H. Wang, Cobalt Carbide Nanoprisms for Direct Production of Lower Olefins from Syngas, *Nature*, 2016, **538**(7623), 84–87.
3 S. Ma, S. d. Huang and Z. P. Liu, Dynamic Coordination of Cations and Catalytic Selectivity on Zinc–Chromium Oxide Alloys during Syngas Conversion, *Nat. Catal.*, 2019, **2**(8), 671–677.
4 F. Jiao, J. Li, X. Pan, J. Xiao, H. Li, H. Ma, M. Wei, Y. Pan, Z. Zhou, M. Li, S. Miao, J. Li, Y. Zhu, D. Xiao, T. He, J. Yang, F. Qi, Q. Fu and X. Bao, Selective Conversion of Syngas to Light Olefins Downloaded From, *Science*, 2016, **351**(6277), 1065.
5 C. Palmer, D. C. Upham, S. Smart, M. J. Gordon, H. Metiu and E. W. McFarland, Dry Reforming of Methane Catalysed by Molten Metal Alloys, *Nat. Catal.*, 2020, **3**(1), 83–89.
6 Y. Song, E. Ozdemir, S. Ramesh, A. Adishev, S. Subramanian, A. Harale, M. Albuali, B. A. Fadhel, A. Jamal, D. Moon, S. H. Choi and C. T. Yavuz, Dry Reforming of Methane by Stable Ni–Mo Nanocatalysts on Single-Crystalline MgO, *Science*, 2020, **367**(6479), 777–781.
7 M. Akri, S. Zhao, X. Li, K. Zang, A. F. Lee, M. A. Isaacs, W. Xi, Y. Gangarajula, J. Luo, Y. Ren, Y. T. Cui, L. Li, Y. Su, X. Pan, W. Wen, Y. Pan, K. Wilson, L. Li, B. Qiao, H. Ishii, Y. F. Liao, A. Wang, X. Wang and T. Zhang, Atomically Dispersed Nickel as Coke-Resistant Active Sites for Methane Dry Reforming, *Nat. Commun.*, 2019, **10**, 5181.
8 F. Cheng, X. Duan and K. Xie, Dry Reforming of CH_4/CO_2 by Stable Ni Nanocrystals on Porous Single-Crystalline MgO Monoliths at Reduced Temperature, *Angew. Chem., Int. Ed.*, 2021, **60**(34), 18792–18799.
9 F. Solymosi, P. Tolmacsov and T. S. Zakar, Dry Reforming of Propane over Supported Re Catalyst, *J. Catal.*, 2005, **233**(1), 51–59.
10 B. Yan, X. Yang, S. Yao, J. Wan, M. N. Z. Myint, E. Gomez, Z. Xie, S. Kattel, W. Xu and J. G. Chen, Dry Reforming of Ethane and Butane with CO_2 over $PtNi/CeO_2$ Bimetallic Catalysts, *ACS Catal.*, 2016, **6**(11), 7283–7292.
11 X. Li, B. Yan, S. Yao, S. Kattel, J. G. Chen and T. Wang, Oxidative Dehydrogenation and Dry Reforming of N-Butane with CO_2 over NiFe Bimetallic Catalysts, *Appl. Catal., B*, 2018, **231**, 213–223.
12 E. Gomez, Z. Xie and J. G. Chen, The Effects of Bimetallic Interactions for CO_2-Assisted Oxidative Dehydrogenation and Dry Reforming of Propane, *AIChE J.*, 2019, **65**(8), 1–12.
13 L. B. Råberg, M. B. Jensen, U. Olsbye, C. Daniel, S. Haag, C. Mirodatos and A. O. Sjåstad, Propane Dry Reforming to Synthesis Gas over Ni-Based Catalysts: Influence of Support and Operating Parameters on Catalyst Activity and Stability, *J. Catal.*, 2007, **249**(2), 250–260.
14 J. Dong, Y. Song, S. Huang, P. Chang and Z. Lai, Dry Reforming of Propane over PtNi Bimetallic Catalysts to Produce Syngas, *ChemistrySelect*, 2025, **10**(34), e03739.
15 F. Solymosi, P. Tolmacsov and K. Kedves, CO_2 Reforming of Propane over Supported Rh, *J. Catal.*, 2003, **216**(1–2), 377–385.
16 D. Sutton, J.-F. Moisan and J. R. H. Ross, Kinetic Study of CO_2 Reforming of Propane over Ru/Al_2O_3, *Catal. Lett.*, 2001, **75**(3–4), 175–181.
17 J. Niu, Y. Wang, S. E. Liland, S. K. Regli, J. Yang, K. R. Rout, J. Luo, M. Rønning, J. Ran and D. Chen, Unraveling Enhanced Activity, Selectivity, and Coke Resistance of Pt-Ni Bimetallic Clusters in Dry Reforming, *ACS Catal.*, 2021, **11**(4), 2398–2411.

18 A. Siahvashi and A. A. Adesina, Synthesis Gas Production via Propane Dry(CO_2) Reforming: Influence of Potassium Promotion on Bimetallic Mo-Ni/Al_2O_3, *Catal. Today*, 2013, **214**, 30–41.
19 A. Siahvashi, D. Chesterfield and A. A. Adesina, Propane CO_2 (Dry) Reforming over Bimetallic Mo-Ni/Al_2O_3 Catalyst, *Chem. Eng. Sci.*, 2013, **93**, 313–325.
20 A. Olafsen, C. Daniel, Y. Schuurman, L. B. Råberg, U. Olsbye and C. Mirodatos, Light Alkanes CO_2 Reforming to Synthesis Gas over Ni Based Catalysts, *Catal. Today*, 2006, **115**(1–4), 179–185.
21 M. S. P. Sudhakaran, M. M. Hossain, G. Gnanasekaran and Y. S. Mok, Dry Reforming of Propane over γ-Al_2O_3 and Nickel Foam Supported Novel $SrNiO_3$ Perovskite Catalyst, *Catalysts*, 2019, **9**(68), 1–18.
22 K. Liu, F. Xing, Y. Xiao, N. Yan, K. I. Shimizu and S. Furukawa, Development of a Highly Stable Ternary Alloy Catalyst for Dry Reforming of Methane, *ACS Catal.*, 2023, **13**(6), 3541–3548.
23 M. B. Jensen, L. B. Råberg, A. Olafsen Sjåstad and U. Olsbye, Mechanistic Study of the Dry Reforming of Propane to Synthesis Gas over a Ni/Mg(Al)O Catalyst, *Catal. Today*, 2009, **145**(1–2), 114–120.
24 F. Barzegari, M. Rezaei, M. Kazemeini, F. Farhadi and A. R. Keshavarz, Effect of Rare-Earth Promoters(Ce, La, Y and Zr) on the Catalytic Performance of NiO-MgO-SiO_2 Catalyst in Propane Dry Reforming, *Mol. Catal.*, 2022, **522**(112235), 1–13.
25 M. Ahadzadeh, S. M. Alavi, M. Rezaei and E. Akbari, Propane Dry Reforming over Highly Active NiO-MgO Solid Solution Catalyst for Synthesis Gas Production, *Mol. Catal.*, 2022, **524**(112325), 1–11.
26 F. Xing, J. Jeon, T. Toyao, K. I. Shimizu and S. Furukawa, A Cu-Pd Single-Atom Alloy Catalyst for Highly Efficient NO Reduction, *Chem. Sci.*, 2019, **10**(36), 8292–8298.
27 F. Xing, Y. Nakaya, S. Yasumura, K. Shimizu and S. Furukawa, Ternary Platinum–Cobalt–Indium Nanoalloy on Ceria as a Highly Efficient Catalyst for the Oxidative Dehydrogenation of Propane Using CO_2, *Nat. Catal.*, 2022, **5**(1), 55–65.
28 F. Xing and S. Furukawa, Metallic Catalysts for Oxidative Dehydrogenation of Propane Using CO_2, *Chem. – Eur. J.*, 2023, **29**(3), e202202173.
29 Y. Nakaya and S. Furukawa, Catalysis of Alloys: Classification, Principles, and Design for a Variety of Materials and Reactions, *Chem. Rev.*, 2023, **123**(9), 5859–5947.
30 J. Dong, D. Li, Y. Zhang, P. Chang and Q. Jin, Insights into the CeO_2 Facet-Depended Performance of Propane Oxidation over Pt-CeO_2 Catalysts, *J. Catal.*, 2022, **407**, 174–185.
31 J. Dong, Y. Zhang, D. Li, A. Adogwa, S. Huang, M. Yang, J. Yang and Q. Jin, Reaction-Driven Evolutions of Pt States over Pt-CeO_2 Catalysts during CO Oxidation, *Appl. Catal., B*, 2023, **330**, 122662.
32 H. Lei, N. Zhang, S. Hu, F. Peng, J. Zhou, J. He, L. Zhang, H. Wang, C. Ma, H. Yan, K. Shimizu and J. Zeng, Thermally Triggered Redox Flexibility of Pt/CeO_2 Cluster Catalyst Against In-Situ Atomic Redispersion, *Angew. Chem.*, 2025, **64**(31), e202509239.
33 Á. Szamosvölgyi, Á. Pitó, A. Efremova, K. Baán, B. Kutus, M. Suresh, A. Sápi, I. Szenti, J. Kiss, T. Kolonits, Z. Fogarassy, B. Pécz, Á. Kukovecz and Z. Kónya, Optimized Pt-Co Alloy Nanoparticles for Reverse Water-Gas Shift Activation of CO_2, *ACS Appl. Nano Mater.*, 2024, **7**(9), 9968–9977.
34 A. Ankudinov and B. Ravel, Real-Space Multiple-Scattering Calculation and Interpretation of x-Ray-Absorption near-Edge Structure, *Phys. Rev. B: Condens. Matter Mater. Phys.*, 1998, **58**(12), 7565–7576.
35 M. D. Segall, P. J. D. Lindan, M. J. Probert, C. J. Pickard, P. J. Hasnip, S. J. Clark and M. C. Payne, First-Principles Simulation: Ideas, Illustrations and the CASTEP Code, *J. Phys.: Condens. Matter*, 2002, **14**, 2717–2744.
36 B. Hammer, L. B. Hansen and J. K. Nørskov, Improved Adsorption Energetics within Density-Functional Theory Using Revised Perdew-Burke-Ernzerhof Functionals, *Phys. Rev. B: Condens. Matter Mater. Phys.*, 1999, **59**(11), 7413–7421.
37 A. Tkatchenko and M. Scheffler, Accurate Molecular van Der Waals Interactions from Ground-State Electron Density and Free-Atom Reference Data, *Phys. Rev. Lett.*, 2009, **102**(7), 073005.
38 K. Hu, M. Wu, S. Hinokuma, T. Ohto, M. Wakisaka, J. I. Fujita and Y. Ito, Boosting Electrochemical Water Splitting: Via Ternary NiMoCo Hybrid Nanowire Arrays, *J. Mater. Chem. A*, 2019, **7**(5), 2156–2164.
39 J. Barzilai and J. M. Borwein, Two-Point Step Size Gradient Methods, *IMA J. Numer. Anal.*, 1988, **8**, 141–148.
40 R. Jana and S. C. Peter, One-Pot Solvothermal Synthesis of Ordered Intermetallic Pt2In3 as Stable and Efficient Electrocatalyst towards Direct Alcohol Fuel Cell Application, *J. Solid State Chem.*, 2016, **242**, 133–139.
41 J. Ye, C. Liu and Q. Ge, A DFT Study of Methanol Dehydrogenation on the PdIn(110) Surface, *Phys. Chem. Chem. Phys.*, 2012, **14**(48), 16660–16667.
42 N. Govind, M. Petersen, G. Fitzgerald, D. King-Smith and J. Andzelm, A Generalized Synchronous Transit Method for Transition State Location, *Comput. Mater. Sci.*, 2003, **28**(2), 250–258.
43 T. A. Halgren and W. N. Lipscomb, The Synchronous-Transit Method for Determining Reaction Pathways and Locating Molecular Transition States, *Chem. Phys. Lett.*, 1977, **49**(2), 225–232.

